

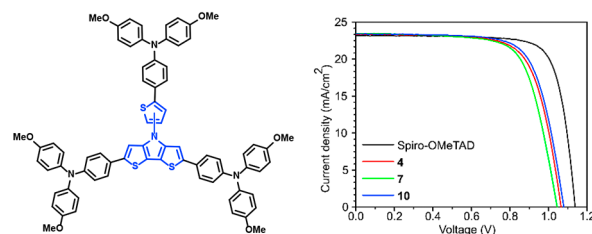
# Broadly Applicable Synthesis of Heteroarylated Dithieno[3,2-*b*:2',3'-*d*]pyrroles for Advanced Organic Materials – Part 2: Hole-Transporting Materials for Perovskite Solar Cells

Masaud Almalki<sup>a</sup> Christoph Lorenz<sup>b</sup>Astrid Vogt<sup>b</sup>Anwar Alanazi<sup>a</sup> Jing Gao<sup>a</sup> Shaik M. Zakeeruddin<sup>a</sup> Peter Bäuerle<sup>\* a</sup> Felix T. Eickemeyer<sup>\* a</sup> Michael Grätzel<sup>\* a</sup>

<sup>a</sup> Laboratory of Photonics and Interfaces, Institute of Chemical Sciences and Engineering, École Polytechnique Fédérale de Lausanne (EPFL), Station 6, 1015 Lausanne, Switzerland

<sup>b</sup> Institute of Organic Chemistry II and Advanced Materials, University of Ulm, Albert-Einstein-Allee 11, 89081 Ulm, Germany

\* peter.baeuerle@uni-ulm.de, felix.eickemeyer@epfl.ch, michael.graetzel@epfl.ch



Received: 12.08.2022

Accepted after revision: 27. 10. 2022

DOI: 10.1055/a-1972-5978; Art ID: OM-2022-08-0032-OA

License terms:

© 2023. The Author(s). This is an open access article published by Thieme under the terms of the Creative Commons Attribution-NonDerivative-NonCommercial License, permitting copying and reproduction so long as the original work is given appropriate credit. Contents may not be used for commercial purposes, or adapted, remixed, transformed or built upon. (<https://creativecommons.org/licenses/by-nc-nd/4.0/>)

**Abstract** Functionalization of heteroarylated dithieno[3,2-*b*:2',3'-*d*]pyrroles (DTPs) by triarylamine was elaborated to result in novel hole-transport materials (HTMs) for perovskite solar cells. The new HTMs showed promising photovoltaic performance with efficiencies exceeding 18%. A thorough investigation of the electronic and optoelectronic properties revealed that the main efficiency loss mechanisms are not related to the pristine HTM materials but to the suboptimal interface passivation and HTM doping. We provide an optimization strategy for those device fabrication factors, which could render these new materials a potential replacement of current state-of-the-art HTMs.

**Key words:** organic materials, conjugated molecules, dithienopyrroles, hole-transport materials, perovskite solar cells, optoelectronic properties

## Introduction

After having introduced a novel synthesis method of N-heteroarylated dithieno[3,2-*b*:2',3'-*d*]pyrroles (DTPs) by microwave-assisted Cu-catalyzed coupling of parent *H*-DTP with 5- and 6-membered heteroaromatic halides in the first part, we now apply this technique to synthesize new hole-transport materials (HTMs) for perovskite solar cells (PSCs).<sup>1</sup>

PSCs have shown a remarkable increase in power conversion efficiency (PCE) from 3.8%<sup>2</sup> in 2009 to 25.7%<sup>3</sup> recently, which has become close to the record efficiency for single-crystal silicon solar cells (26.1%).<sup>3</sup> Hybrid organic–inorganic perovskites have the chemical formula AMX<sub>3</sub>. They adapt a pseudo-cubic structure made of corner-sharing octahedra MX<sub>6</sub> consisting of a divalent cation M (e.g. Pb<sup>2+</sup> or Sn<sup>2+</sup>) and monovalent anions X (e.g. Cl<sup>−</sup>, Br<sup>−</sup>, or I<sup>−</sup>) with an A cation (e.g. MA<sup>+</sup>, FA<sup>+</sup>, and Cs<sup>+</sup>) in the cuboctahedral cavities.<sup>4–7</sup> They possess extraordinary optoelectronic properties such as high absorption coefficient,<sup>8,9</sup> small exciton binding energy,<sup>10,11</sup> long charge carrier diffusion lengths<sup>12,13</sup> and high charge carrier mobility.<sup>14</sup> State-of-the-art PSCs with the n-i-p architecture employ SnO<sub>2</sub> or TiO<sub>2</sub> as an electron transport layer and spiro-OMeTAD as a HTM.<sup>15,16</sup> A major disadvantage of spiro-OMeTAD is the low glass transition temperature decreasing the thermal stability.<sup>17</sup> Many new organic HTMs have been developed in recent years<sup>18–21</sup> but the highest efficient PSCs still rely on spiro-OMeTAD.

Therefore, there is still a need to further develop new, stable HTMs, which eventually replace spiro-OMeTAD in particular for commercial applications. DTP is an electron-rich molecule, which is frequently implemented with suitable functionalization as a semiconducting material in organic electronic devices.<sup>22–24</sup> As HTM in PSCs, there are only a few examples described in the literature. One is represented by a N-(2-thienyl)-substituted DTP, which was used as the central part of a larger co-oligomer.<sup>25,26</sup> In another work, a DTP-based HTM bearing a p-methoxyphenyl residue at the DTP nitrogen was synthesized and investigated by Martin, Nazeeruddin et al.<sup>27</sup> Very recently, DTP was used in combi-

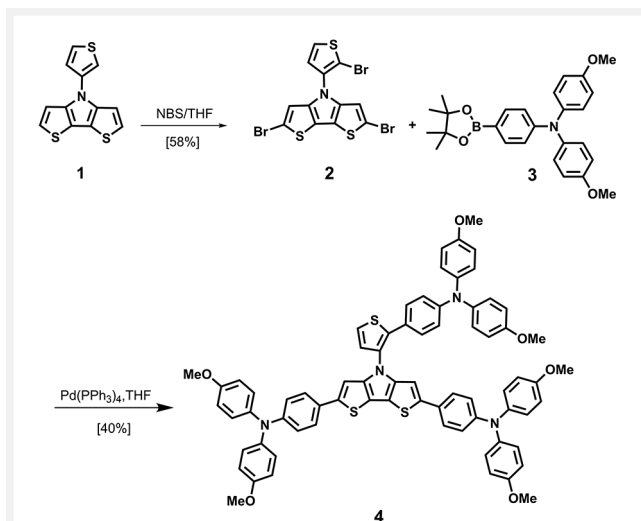
nation with a spiro-type backbone to increase molecular planarity.<sup>28</sup> DTP derivatives are less complex to synthesize than spiro compounds; in this respect, we have recently elaborated and disclosed straightforward direct arylation and heteroarylation procedures to introduce directly  $\pi$ -conjugated aromatic and heteroaromatic substituents at the central DTP-nitrogen.<sup>1,29</sup>

Herein, we now describe the synthesis and characterization of three novel DTPs, which were functionalized with triarylamine units to result in advanced HTMs for PSCs. We present a thorough characterization of these new HTMs in PSCs, which reveals their promising potential for high-performance optoelectronic devices.

## Results and Discussion

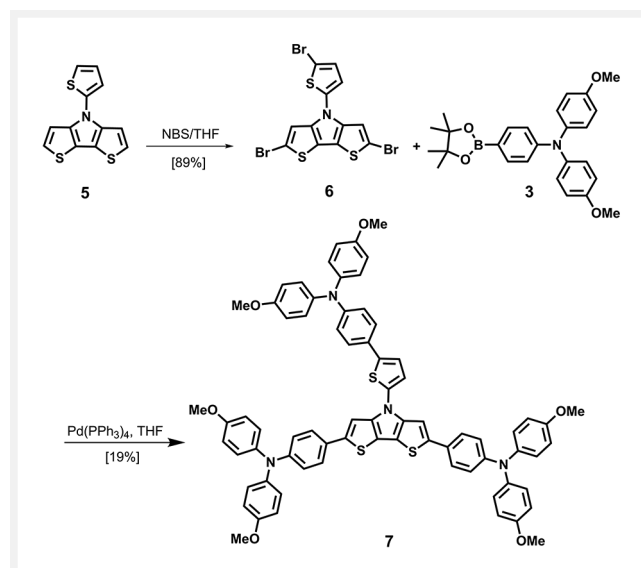
### Synthesis of novel HTMs

*N*-Thienyl-substituted DTPs **1** and **5**<sup>1</sup> were further functionalized for application as HTMs in PSCs. Thus, 3-thienyl-DTP **1** was first brominated with three equivalents of *N*-bromosuccinimide (NBS) in THF to yield triply brominated 3-thienyl-DTP **2** in 58% yield, which had to be separated chromatographically from a simultaneously formed isomer. Brominated 3-thienyl-DTP **2** was subsequently reacted in a three-fold Suzuki-type coupling with Pd(PPh<sub>3</sub>)<sub>4</sub> as a catalyst with triarylamine boronic ester **3**, which was efficiently prepared according to literature procedures,<sup>17</sup> to furnish triarylamine-substituted DTP **4** in 40% yield (Scheme 1).



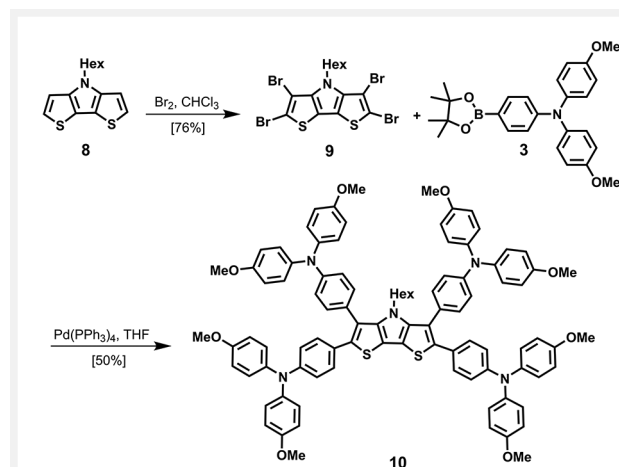
**Scheme 1** Synthesis of HTM **4** starting from 3-thienyl-substituted DTP **1**.

In the same way, isomeric 2-thienyl-DTP **5** was selectively brominated to tribromo derivative **6** in 89% yield, which was subsequently coupled with boronic ester **3** to related triarylamine-DTP **7** in a yield of 19% (Scheme 2).



**Scheme 2** Synthesis of HTM **7** starting from 2-thienyl-substituted DTP **5**.

Furthermore, and for comparison, tetraarylated DTP **10** was synthesized as a potential HTM from tetrabrominated *N*-hexylated DTP **9** with triarylamine boronic ester **7** in a fourfold Suzuki-type coupling with Pd(PPh<sub>3</sub>)<sub>4</sub> as a catalyst in 50% yield (Scheme 3). Beforehand, tetrabromo-DTP **9** was prepared in 76% yield from *N*-hexyl-DTP **8**<sup>24b</sup> with elemental bromine in chloroform. The prepared heteroarylated



**Scheme 3** Synthesis of HTM **10** starting from *N*-hexyl-substituted DTP **8**.

DTPs **2**, **4**, **6**, **7**, **9**, and **10** were fully characterized and their purity and structures confirmed by HPLC, NMR spectroscopy (Figures S1–S5), and mass spectrometry (Figures S6–S10).

### Thermal, optical, and redox properties of DTP-based HTM **4**, **7**, and **10**

Differential scanning calorimetry (DSC) and thermal gravimetric analysis (TGA) (Figure S11) were used to determine the thermal properties of HTMs **4**, **7**, and **10**, which are important for processing temperatures and long-term stability of photovoltaic devices. DSC traces of thienyl-DTP-based HTMs **4** and **7** revealed glass transition temperatures of 138 °C and 140 °C, respectively, and no defined melting was visible, most probably due to their amorphous character. In contrast, HTM **10** showed a sharp melting point at 251 °C. These values are higher than the glass transition temperature of spiro-OMeTAD ( $T_g = 125$  °C),<sup>30</sup> which is the most often used HTM in PSCs. The three HTMs are thermally very stable and showed decomposition ranges above 420 °C (@ 95 % mass) measured by TGA.

Optical investigations of the triarylamine-extended DTPs **4**, **7**, and **10** were performed by UV-vis absorption in THF solution and in thin films, which were spin-coated from chloroform solutions. All data are compiled in Table 1 and exemplarily UV-vis spectra of the triarylamine-DTPs in solution are shown in Figure 1a. The UV-vis spectra of triarylamine-DTPs **4** and **7** are dominated by strong main absorption bands in the visible spectrum at 429 and 427 nm, which are strongly red-shifted compared to the basic DTPs **1** and **5**, respectively. We address this band to the  $\pi$ - $\pi^*$  transition of the overall conjugated  $\pi$ -system, in which the DTP unit is extended by the flanked triarylamines. The less intense bands at around 300 nm are jointly assigned to the triarylamine and DTP subchromophores in accordance with the absorption maximum of 299 nm for DTP and 300 nm for bis(4-methoxyphenyl)aniline.<sup>17,31</sup> In the case of triarylamine-DTP **10** with four triarylamine groups, the circumstances are reverse and the latter UV-band is dominating over the  $\pi$ - $\pi^*$

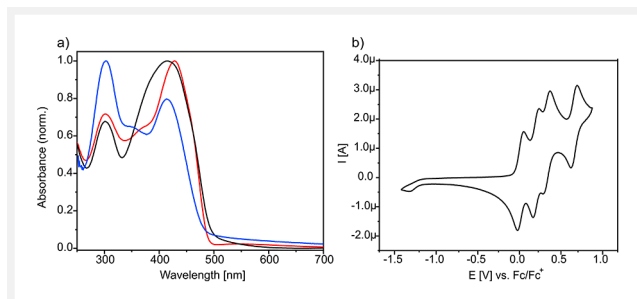


**Figure 1** a) UV-vis absorption spectra of triarylamine-substituted DTP-derivatives **4** (red curve), **7** (black), and **10** (blue) in thin films spin-coated on glass. b) Cyclic voltammogram of triarylamine-DTP **7** in dichloromethane/tetrabutylammonium hexafluorophosphate (0.1 M), 100 mV/s, r.t., potentials vs. ferrocene/ferricenium (Fc/Fc<sup>+</sup>).

band, which is blue-shifted compared to derivatives **4** and **7**. The shape of the corresponding film spectra and location of the maxima are nearly identical to the solution spectra indicating low molecular organization in the solid state and rather amorphous films.

The redox properties of DTP derivatives **4**, **7**, and **10** were studied by means of CV in dichloromethane (DCM) and tetrabutylammonium hexafluorophosphate (0.1 M) as the electrolyte; potentials were referenced against the ferrocene/ferricenium couple (Fc/Fc<sup>+</sup>). In Figure 1b, a representative CV of HTM **7** is shown and data for all derivatives are compiled in Table 1. The CV of **7** showed four successive reversible oxidation waves with half-wave potentials at -0.09, 0.10, 0.56, and 0.82 V corresponding to the formation of stable radical cations up to tetracations. We assume that the two lateral triarylamine subelectrophores are firstly consecutively oxidized to the radical cation (first two waves), then subsequently the third triarylamine pending at the thienyl substituent (third wave). The fourth wave reflects the oxidation of the central DTP unit at a potential comparable to that of core molecule **1**. With slight potential shifts, similar CVs were measured for derivatives **4** and **10** (Figure S12, Table S1). The HOMO energy levels (-4.94 to -5.03 eV) were calculated from the onset of the first oxidation wave assuming a value of -5.1 eV for Fc/Fc<sup>+</sup> vs. vacuum. Corresponding LUMO

**Table 1** Optical and redox data of triarylamine-substituted DTPs **4**, **7**, and **10**

DTP	$\lambda_{\text{abs}}$ [nm] <sup>a</sup>	$\epsilon$ [M <sup>-1</sup> · cm <sup>-1</sup> ]	$E_{\text{g}}^{\text{opt}}$ [eV] <sup>c</sup>	$\lambda_{\text{max}}^{\text{film}}$ [nm] <sup>b</sup>	$E_{1/2}^{\text{Ox1}}$ [V] <sup>d</sup>	$E_{1/2}^{\text{Ox2}}$ [V] <sup>d</sup>	$E_{1/2}^{\text{Ox3}}$ [V] <sup>d</sup>	$E_{1/2}^{\text{Ox4}}$ [V] <sup>d</sup>	HOMO [eV] <sup>e</sup>	LUMO [eV] <sup>f</sup>
<b>4</b>	302 (362), <u>429</u>	79 330	2.59	302, (370) 428	0.03	0.22	0.35	0.70	-5.03	-2.44
<b>7</b>	301, <u>427</u>	84 420	2.59	301, (373) 416	-0.09	0.10	0.56	0.82	-4.94	-2.35
<b>10</b>	<u>300</u> (349), 411	73 340	2.58	303, (347) 413	-0.02	0.18	0.42	0.63	-4.96	-2.38

<sup>a</sup>UV-vis spectra measured in THF, maxima underlined, shoulders in brackets. <sup>b</sup>Films obtained by spin-coating chloroform solutions onto glass slides. <sup>c</sup>Calculated from the onset value of the longest wavelength band by  $E_{\text{g}} = 1240/\lambda_{\text{onset}}$ . <sup>d</sup>Cyclic voltammograms measured in dichloromethane/tetrabutylammonium hexafluorophosphate (0.1 M), scan rate 100 mV · s<sup>-1</sup>, potentials referenced against the ferrocene/ferricenium couple (Fc/Fc<sup>+</sup>). <sup>e</sup>Calculated from the onset value of the oxidation wave; Fc/Fc<sup>+</sup> was set to -5.1 eV vs. vacuum. <sup>f</sup>Calculated by taking the optical gap into account ( $E_{\text{HOMO}} - E_{\text{g}}^{\text{opt}}$ ).

energy levels were calculated taking the optical energy gaps into account and ranged from  $-2.35$  eV to  $-2.44$  eV. These energy levels, which are similar to those of spiro-OMeTAD (HOMO:  $-5.04$  eV, LUMO:  $-2.05$  eV)<sup>17</sup> should allow for application of these derivatives as HTM in PSCs enabling efficient electron blocking and hole transfer from the perovskite layer to the gold counter electrode.

### Photovoltaic properties and solar cell performance

We fabricated PSCs with the layered structure glass/FTO/compact-TiO<sub>2</sub>/mesoscopic-TiO<sub>2</sub>/perovskite/interface passivator/HTM/gold. The perovskite composition used here [FA<sub>0.85</sub>MA<sub>0.1</sub>Cs<sub>0.05</sub>Pb(I<sub>0.97</sub>Br<sub>0.03</sub>)<sub>3</sub>] represents a standard formulation often found in the literature for stable and efficient PSCs.<sup>17,32–35</sup> Octylammonium iodide (OAI) employed as the interface passivator was spin-coated on top of the perovskite film. Subsequently, we spin-coated a solution of the HTMs dissolved in chlorobenzene (CB). As a control experiment we used spiro-OMeTAD, which is the most frequently used HTM in high-performance perovskite devices.<sup>15,36–40</sup> The HTM concentration was 75 mM and we prepared the solutions with and without lithium bistrifluorosulfonyl imide (Li-TFSI) and 4-*tert*-butylpyridine (4-*t*BP) doping. A comprehensive description of the device preparation is detailed in the Experimental Section.

For morphology characterization of the HTM films, we used scanning electron microscopy (SEM). The undoped HTMs feature very thin layers (thickness of around  $\sim 20$  nm) with poor surface coverage due to cracks apparent in the

top-view SEM images (Figure S13). Upon doping, the HTM films revealed pinhole-free compact layers with much larger thicknesses (spiro-OMeTAD: 196 nm, **4**: 196 nm, **7**: 141 nm, and **10**: 143 nm). A cross-section SEM is shown exemplary for HTM **10** in Figure 2a, the respective SEM graphs for the other HTMs can be found in Figure S14. The current density–voltage ( $J$ – $V$ ) curves of devices based on doped HTMs **4**, **7**, **10**, and spiro-OMeTAD, measured under AM1.5 G irradiation, are displayed in Figure 2b. Photovoltaic metrics of four devices for each HTM are summarized in Table 2. HTM **7** reached an average PCE of 17.0%, while HTM **4** yielded an average PCE of 17.7% due to a 30 mV higher  $V_{oc}$  than HTM **7**. HTM **10** achieved a higher PCE of an average 18.1% as a result of a 2% higher fill factor (FF) and 10 mV and 40 mV higher open-circuit voltage ( $V_{oc}$ ) than HTM **4** and **7**, respectively. These values demonstrate that these new DTP-based materials are promising HTMs. However, their device performance under the chosen preparation conditions still lags 10% behind the spiro-OMeTAD PCE, which is mainly due to a 50–90 mV lower  $V_{oc}$  and 6–7% lower FF. Note that the device performances with undoped HTMs are all very similar

**Table 2** PV parameter statistics of four PSCs based on **4**, **7**, **10**, and spiro-OMeTAD; all HTMs were doped as described in the main text

HTM	$V_{oc}$ (V)	$J_{sc}$ (mA/cm <sup>2</sup> )	FF (%)	PCE (%)
<b>4</b>	$1.07 \pm 0.01$	$23.3 \pm 0.2$	$69 \pm 2$	$17.7 \pm 0.3$
<b>7</b>	$1.04 \pm 0.02$	$23.5 \pm 0.4$	$69 \pm 2$	$17.0 \pm 0.2$
<b>10</b>	$1.08 \pm 0.01$	$23.4 \pm 0.4$	$71 \pm 1$	$18.1 \pm 0.3$
Spiro-OMeTAD	$1.13 \pm 0.01$	$23.4 \pm 0.3$	$77 \pm 2$	$20.1 \pm 0.3$

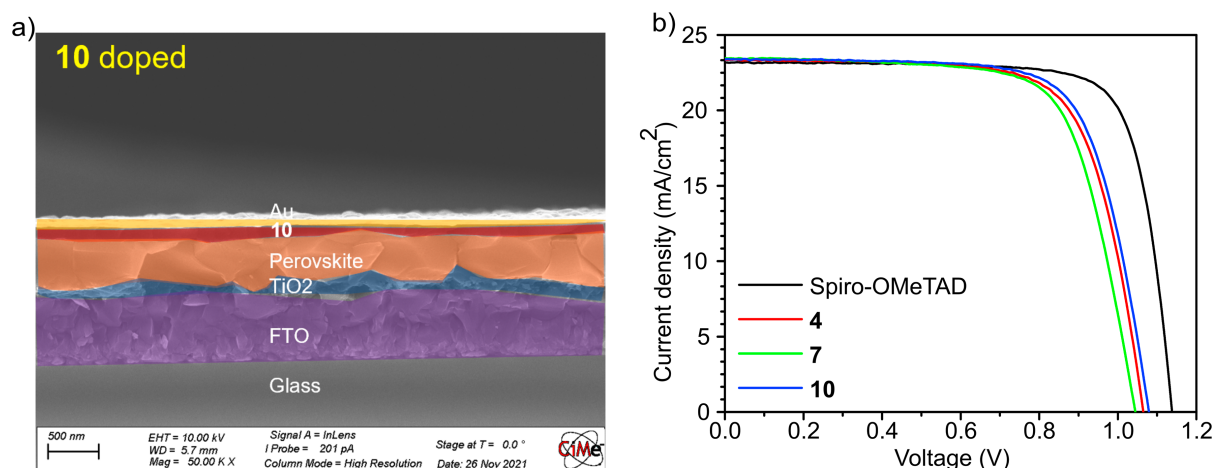


**Figure 2** (a) Cross-sectional SEM graph of a PSC with doped HTM **10** (colored in red); (b)  $J$ – $V$  curve for devices made with doped HTMs: **4** (red curve), **7** (green curve), **10** (blue curve), and spiro-OMeTAD (black curve).

but with around 5% PCE much lower than the devices with doped HTMs (see Figure S18 and Table S5) due to the poor HTM film quality; therefore, we focus here on the characterization of the latter. To understand the reasons behind the lower  $V_{oc}$  and FF of the devices with doped HTMs, we carried out in-depth optoelectronic characterizations presented in the following.

## Optoelectronic characterization

In order to explain the reasons behind the differences in  $V_{oc}$ , we carried out steady-state photoluminescence quantum yield (PLQY) measurements. PLQY is the emitted photon flux divided by the absorbed photon flux measured under an open circuit. Under this condition, the emitted photon flux is limited by non-radiative recombination processes. Hence, PLQY measurements are an important technique to probe non-radiative recombination in the bulk absorber film and at interfaces with the transport layers.<sup>41</sup> PLQY measurements of PSC devices are shown in Figure 3a and Table S2. The bare perovskite film deposited on glass showed a PLQY of 3.2%, only limited by bulk and surface recombination. Devices with spiro-OMeTAD yielded a PLQY of 2.2% showing additional non-radiative recombination at the  $TiO_2$ /perovskite and perovskite/spiro-OMeTAD interfaces. Devices based on the new HTMs **4**, **7**, and **10** render PLQYs with less than 1% (0.6%, 0.1%, and 0.9%, respectively) due to increased non-radiative recombination losses at the interface perovskite/HTM.

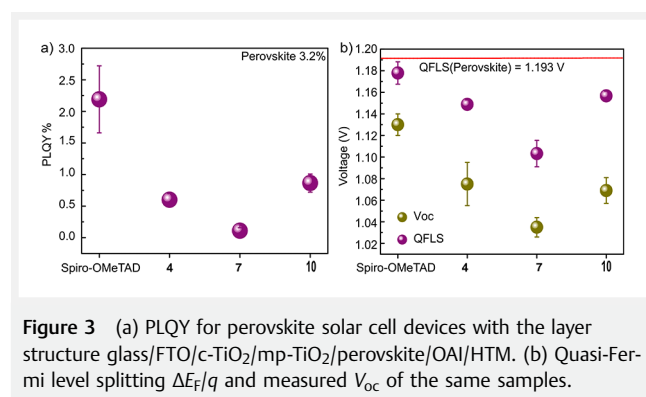


**Figure 3** (a) PLQY for perovskite solar cell devices with the layer structure glass/FTO/c- $TiO_2$ /mp- $TiO_2$ /perovskite/OAI/HTM. (b) Quasi-Fermi level splitting  $\Delta E_F/q$  and measured  $V_{oc}$  of the same samples.

From PLQY the quasi-Fermi level splitting  $\Delta E_F$  can be determined (details can be found in the Supporting Information, SI).<sup>42</sup>  $\Delta E_F/q$ , where  $q$  is the elementary charge, is the internal voltage of the absorber layer and represents the maximum  $V_{oc}$ , which a solar cell with this absorber layer can achieve if there are no additional losses. In Figure 3b and Table S3, we show the comparison between  $\Delta E_F/q$  and the measured steady-state  $V_{oc}$  of the same cell.  $\Delta E_F/q$  and  $V_{oc}$  follow the same trend for all HTMs, which shows that the  $V_{oc}$  differences originate from differences in non-radiative re-

combination. The offset between  $\Delta E_F/q$  and  $V_{oc}$  is a result of energy level offsets between the conduction band of  $TiO_2$  and perovskite and the valence bands of perovskite and HTM in combination with non-radiative recombination (Figure S15).<sup>43</sup>

## Mobility and conductivity measurements

Finally, we address the difference of the FFs between the new HTMs and spiro-OMeTAD. For devices with high charge carrier mobility like PSCs, the FF is determined mainly by two mechanisms, non-radiative recombination losses,<sup>44–49</sup> which have been studied in the previous section, and by the series resistance  $R_s$ . To determine the series resistance caused by the HTM layers, we measured their conductivities. For this, we deposited the HTMs on glass substrates and compared their dark conductivities with spiro-OMeTAD. The details of the film fabrication and measurement can be found in the Experimental Section and in SI, respectively. The results of the conductivity measurements are shown in Figure 4 and Table S4. For the as-deposited films, we obtained a conductivity of  $4.7 \cdot 10^{-7}$  S/cm with spiro-OMeTAD, which is in good agreement with literature data.<sup>50–53</sup> For HTMs **4** and **7** the conductivities are similar to this value, for **10** it is almost an order of magnitude lower.

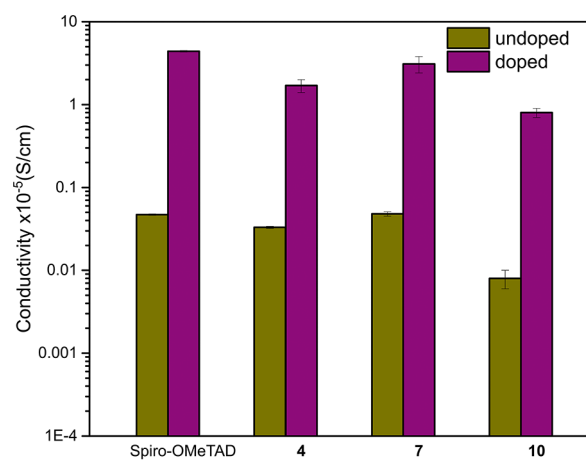


**Figure 4** Conductivities measured in the dark for spiro-OMeTAD, **4**, **7**, and **10** with and without doping. The dopants used were Li-TFSI and 4-*t*BP with a molar ratio of HTM:LiTFSI:4-*t*BP = 1:0.5:3.

Since in optoelectronic devices conductivities significantly higher than those determined above are needed, spiro-OMeTAD is usually doped and the most frequently used dopants are Li-TFSI and 4-*t*BP with a molar ratio of spiro-OMeTAD:Li-TFSI:4-*t*BP = 1:0.5:3, which is also the recipe used for the devices with the different HTMs presented



above. Therefore, we also measured the conductivities of the doped HTM films. For doped spiro-OMeTAD, we obtained a conductivity of  $4.4 \cdot 10^{-5}$  S/cm, which is similar to published values.<sup>54–61</sup> HTM **7** has shown a 30% lower conductivity ( $3.1 \cdot 10^{-5}$  S/cm), **4** and **10** yielded a more than 2 times and 5 times lower conductivity ( $1.7 \cdot 10^{-5}$  S/cm and  $0.8 \cdot 10^{-5}$  S/cm), respectively. The series resistance, which is calculated as the quotient of film thickness and conductivity, is  $1.3 \Omega \text{ cm}^2$  for the spiro-OMeTAD layer,  $3.4 \Omega \text{ cm}^2$  for **4**,  $1.4 \Omega \text{ cm}^2$  for **7**, and  $5.0 \Omega \text{ cm}^2$  for **10**. Hence,  $R_s$  is significantly higher for **4** and **10** compared to spiro-OMeTAD.

To understand the reasons behind the difference in conductivities, we measured the mobility of the best performing new HTM **10** and spiro-OMeTAD using the space-charged-limited current technique. We used a hole-only device (Figure S17), where we first deposited a very thin electron blocking layer (PEDOT:PSS) on indium tin oxide (ITO) substrates. The HTMs were then deposited on top of PEDOT:PSS at varying film thicknesses; gold was finally thermally evaporated on the HTMs as the top contact layer. The details of experimental procedures and the model used for calculation can be found in the SI. The new HTM **10** showed a mobility of  $5.1 \cdot 10^{-5} \text{ cm}^2/\text{Vs}$ , which is in the same range as the mobility of spiro-OMeTAD ( $7.6 \cdot 10^{-5} \text{ cm}^2/\text{Vs}$ ). However, the conductivity of **10** is significantly lower than that of spiro-OMeTAD. The reason for this is the significantly lower hole concentration  $n = \sigma/\mu q$ , where  $\sigma$  is the conductivity,  $\mu$  the mobility and  $q$  the elementary charge as shown in Table 3.

**Table 3** Conductivity, mobility, and hole concentration for doped HTMs.

HTM	Conductivity [ $10^{-5}$ S/cm]	Mobility [ $10^{-5} \text{ cm}^2/\text{V} \cdot \text{s}$ ]	Hole concentration [ $10^{18} \cdot \text{cm}^{-3}$ ]
<b>10</b>	$0.8 \pm 0.1$	$5.1 \pm 1.2$	$0.97 \pm 0.4$
Spiro-OMeTAD	$4.4 \pm 0.1$	$7.6 \pm 1.2$	$3.6 \pm 0.8$

## Discussion

We now want to discuss the potential of the new HTMs for efficient PSCs in comparison to the “gold standard” spiro-OMeTAD. The three main properties of an HTM determining the performance of a PSC are energy level alignment, non-radiative recombination at the perovskite/HTM interface, and conductivity. As for the energy-level alignment, the HOMO energy levels of the new HTMs are as well suited for PSCs (Figure S15) like spiro-OMeTAD since they are very similar. As for the second property, we have shown that the lower  $V_{oc}$  for the new HTMs in comparison to spiro-OMeTAD is mainly due to lower PLQY, i.e., significantly higher defect-assisted non-radiative recombination at the interface with

perovskite. These devices used *n*-OAI as the interface passivation agent. PLQYs for devices without OAI are about 1 order of magnitude lower (Table S2) than those for the devices with OAI, hence PLQY depends less critically on the HTM as such than on the actual interface passivation. OAI is a standard passivation agent for the interface perovskite/spiro-OMeTAD,<sup>62,63</sup> but it is not necessarily the optimal passivator for the new HTMs presented here. It is not unlikely that there are better passivators that could increase PLQY and  $V_{oc}$  to the same level as for spiro-OMeTAD. There are many examples for alternative interface passivators in the literature which would be a good starting point to optimize PSCs with the new HTMs.<sup>17,34,64</sup> The enhanced non-radiative recombination at the interface between perovskite and the new HTMs is also one of the reasons for the lower FFs.<sup>44–49</sup> In addition, we have shown that HTMs **4** and **10** showed higher series resistance in comparison to spiro-OMeTAD. Since **10** showed the highest device performance, we further investigated the reason for the higher series resistance by mobility measurements. We have seen that although the conductivity of HTM **10** is significantly lower than that of spiro-OMeTAD, the mobilities of the two HTMs are similar. This can be attributed to a four times lower hole concentration (FCC) of HTM **10**. FCC is directly related to the oxidized HTM concentration, which is induced by doping. The doping used here is optimized for spiro-OMeTAD<sup>65</sup> and it is obviously not as effective as for HTM **10**. It is well possible that with an individually adjusted doping, e.g., through optimized doping concentrations or other HTM oxidation strategies, the conductivity of **10** and also of the other new HTMs could reach the same level as spiro-OMeTAD. In that way, higher device FFs comparable to spiro-OMeTAD are attainable.

## Conclusions

In summary, we have presented synthesis and characterization of novel HTMs **4**, **7**, and **10**, which are based on N-thienylated and hexylated DTPs **1**, **5**, and **8**, respectively, and were tailored for PSCs. The energy levels of the frontier orbitals, which were determined from optoelectronic data, were found to be suitable for the implementation in PSCs. The new HTMs applied in a PSC showed a promising performance with PCEs exceeding 18%.

A thorough optoelectronic characterization was carried out via PLQY, conductivity, and mobility measurements. These investigations revealed that the main loss mechanisms behind the lower performance compared to spiro-OMeTAD are related to passivation of the perovskite/HTM interface and HTM doping. These are all device fabrication factors not directly related to the new HTM structures. By optimizing the interface passivation with the many recently developed passivators and in addition by applying a doping

strategy specifically adjusted to the new HTMs, these new materials have the same device efficiency potential as the state-of-the-art HTMs. In addition, due to a higher thermal stability than spiro-OMeTAD, they have even the potential for higher device stability which will be the focus of future investigations.

## Experimental Section

### Instruments and methods

NMR spectra were recorded on an Avance 400 ( $^1\text{H}$  NMR 400 MHz,  $^{13}\text{C}$  NMR 101 MHz) or a Bruker AMX 500 spectrometer ( $^1\text{H}$  NMR 500 MHz,  $^{13}\text{C}$  NMR 125 MHz). Chemical shifts ( $\delta$ ) are reported in ppm using residual solvent protons ( $^1\text{H}$  NMR:  $\delta_{\text{H}} = 7.26$  for  $\text{CDCl}_3$ ;  $\delta_{\text{H}} = 3.58$  for THF- $d_8$ ;  $^{13}\text{C}$  NMR:  $\delta_{\text{C}} = 77.2$  for  $\text{CDCl}_3$ ;  $\delta_{\text{C}} = 67.57$  for THF- $d_8$ ) as the internal standard. The splitting patterns are designated as follows: s (singlet), d (doublet), t (triplet), and m (multiplet). Coupling constants  $J$  relate to proton–proton couplings and assignments were made according to the nomenclature numbering scheme. Thin layer chromatography was carried out on aluminum plates, precoated with silica gel, Merck Si60 F254. Preparative column chromatography was performed on glass columns packed with silica gel (particle size 40–63  $\mu\text{m}$ ) from Macherey-Nagel or aluminium oxide, Merck 90 active basic, particle size 63–200  $\mu\text{m}$ . HPLC was performed on a Shimadzu CBM-20A equipped with an SPD-20A UV-Vis detector and an LC-8A solvent delivery system using a Macherey-Nagel column (Nucleosil 100–5  $\text{NO}_2$ ). Melting points were determined using a Büchi Melting Point B-545 (not corrected) or a Mettler Toledo DSC 823e under argon flow (heating rate 10  $^\circ\text{C}/\text{min}$ ). Thermogravimetric analyses were carried out with a TGA/SDTA 851e from Mettler Toledo. GC-MS measurements were performed on a Shimadzu GCMS-QP2010 SE equipped with an Optima 5MS column (30 m  $\times$  0.25 mm) from Macherey-Nagel. High-resolution MALDI mass spectra were recorded on a Bruker Solarix using trans-2-[3-(4-*tert*-butylphenyl)-2-methyl-2-propenylidene]malononitrile (DCTB) as the matrix. High-resolution APCI (Atmospheric pressure chemical ionization) spectra were recorded on a Bruker Solarix using acetonitrile as the solvent.

Optical measurements in solution were carried out in 1 cm cuvettes with Merck Uvasol grade solvents. Absorption spectra were recorded on a Shimadzu UV-3600i Plus UV-vis-nir spectrophotometer. UV-vis absorption spectra of films (spin-coated from chloroform solution onto a glass slide) were recorded on a Perkin Elmer Lambda 19 spectrometer. CV experiments were performed with a computer-controlled Autolab PGSTAT30 potentiostat in a three-electrode single-compartment cell (3 mL). The platinum working electrode consisted of a platinum wire sealed in a

soft glass tube with a surface of  $A = 0.785 \text{ mm}^2$ , which was polished down to 0.25  $\mu\text{m}$  with Buehler polishing paste prior to use to guarantee reproducible surfaces. The counter electrode consisted of a platinum wire and the reference electrode was an Ag/AgCl reference electrode. All potentials were internally referenced to the ferrocene/ferricenium couple ( $\text{Fc}/\text{Fc}^+$ ). For the measurements, concentrations of  $10^{-3} \text{ M}$  of the electroactive species were used in freshly distilled and deaerated DCM (Lichrosolv, Merck) purified with a Braun MB-SPS-800. Tetrabutylammonium hexafluorophosphate (TBAHPF; Sigma-Aldrich, recrystallized twice from ethanol) was applied as the supporting electrolyte in a concentration of 0.1 M and the solution was blanketed with argon during the measurements.

**Photovoltaic performance measurements:** Current–voltage characteristics were recorded under ambient temperature and air conditions. The PSCs were measured using a 300-W Xenon light source (Sol3A) from Newport. The spectral mismatch between AM 1.5 G and the solar simulator was calibrated by a Schott K113 Tempax filter (Prazosopms Glas & Optik GmbH). A silicon photodiode was used as a light intensity calibrator for each measurement. Keithley 2400 was used for the current–voltage scan by applying an external voltage bias and measuring the response current with a scan rate of 50 mV/s. The cells were masked with a black metal mask with an area of 0.16  $\text{cm}^2$ . Stabilized quasi-steady-state  $V_{\text{OC}}$  was obtained after 1 min exposure of the devices under 1 sun simulated illumination conditions.

**SEM measurements:** Top view and cross-sectional SEM measurements were recorded using a high-resolution scanning electron microscope (GeminiSEM 300).

**PLQY measurements:** PLQY was measured using an integrating sphere (Fluorolog, Horiba JobinYvon), an Andor Kymera 193i spectrograph, and a 660 nm continuous-wave laser (OBIS, Coherent) set at 1-sun equivalent photon flux (1.1  $\mu\text{m}$  beam full-width half-maximum, 632  $\mu\text{W}$ ); photoluminescence was collected at normal incidence using a 0.1 NA, 110  $\mu\text{m}$ -diameter optical fiber. For the absolute spectral calibration of the PLQY measurement system, we used a radiometrically calibrated halogen lamp (HL-3 plus CAL from Ocean Optics).

### Materials

**Chemicals for synthesis:** THF, DCM, and *n*-hexane were purchased from Sigma Aldrich, petroleum ether (PE) from VWR/Avantor sciences and were purified by an MB SPS-800 solvent purification equipment from MBraun. NBS and tetrakis(triphenylphosphine)palladium(0) were purchased from Sigma-Aldrich. Tripotassium phosphate was purchased from Sigma-Aldrich and magnesium sulfate from Grüssing GmbH. 4-(Thien-3'-yl)-4H-dithieno[3,2-*b*:2',3'-*d*]pyrrole **1**,<sup>24</sup> 4-(thien-2'-yl)-4H-dithieno[3,2-*b*:2',3'-*d*]pyrrole **5**,<sup>24</sup> 4-

methoxy-*N*-(4-methoxyphenyl)-*N*-(4-(4,4,5,5-tetramethyl-1,3,2-dioxaborolan-2-yl)phenyl)aniline **3**,<sup>66</sup> *N*-hexyl-4*H*-dithieno[3,2-*b*:2',3'-*d*]pyrrole **8**,<sup>67</sup> and *N*-hexyl-2,3,5,6-tetrabromo-4*H*-dithieno[3,2-*b*:2',3'-*d*]pyrrole **9**<sup>24b</sup> were internally synthesized according to literature-known procedures.

**Chemicals for physical investigations:** Conductive fluorine-doped tin oxide (FTO) coated glass (10 ohms/sq) was purchased from Nippon Sheet Glass. Cesium iodide (CsI) was purchased from TCI Co. Ltd., lead iodide (PbI<sub>2</sub>) was purchased from Alfa Co. Ltd. Formamidinium iodide (FAI), methylammonium bromide (MABr), and titanium dioxide paste (30 NR-D) were purchased from Greatcell Solar. 2,2',7,7'-Tetrakis[*N,N*-di(4-methoxyphenyl)amino]-9,9'-spirobifluorene (spiro-OMeTAD) was purchased from Xi'an Polymer Light Technology Corp. Ultradry dimethylformamide (DMF), ultradry dimethyl sulfoxide (DMSO), and ultradry CB were purchased from Acros. Lithium bistrifluoromethyl sulfonate (Li-TFSI), zinc powder, acetyl acetone, phenylethylamine, 4-*tert*-butylpyridine (4-*t*BP), and titanium diisopropoxide bis(acetylacetonate) 75 wt% in IPA were purchased from Sigma-Aldrich. All the chemicals were used as received without further purification.

## Device fabrication

**Substrate preparation:** An etched FTO conducting glass was cleaned using Hellmanex (2%, deionized water), acetone and ethanol by sonicating for 15 min for each solvent consecutively. After drying with compressed air, the glass was finally treated by UV-ozone for 15 min. A 20–40 nm compact TiO<sub>2</sub> layer was deposited on top of FTO glass using the spray pyrolysis method (O<sub>2</sub> as the carrier gas): the substrate was preheated to 450 °C; a precursor solution was 0.6 mL titaniumdiisopropoxide bis(acetylacetonate) (75 wt% in IPA) and 0.4 mL acetyl acetone diluted in 9 mL dry ethanol. After spray pyrolysis, the FTO/c-TiO<sub>2</sub> substrate was heated at 450 °C for 15 min before cooling down to ambient temperature. Next, a mesoporous TiO<sub>2</sub> (m-TiO<sub>2</sub>) layer was deposited on the compact TiO<sub>2</sub> (c-TiO<sub>2</sub>) substrate by spin-coating for 20 s at 4000 rpm with a ramp rate of 2000 rpm·s<sup>-1</sup>, using the commercial TiO<sub>2</sub> paste (30NRD) diluted with anhydrous ethanol at a weight ratio of 1:6. Then the substrates were sintered at 450 °C for 30 min. After the substrates were cooled down, they were moved immediately to a dry air glovebox for completing the following steps.

**Perovskite active layer deposition:** A perovskite precursor solution was prepared by dissolving a mixture of PbI<sub>2</sub> (1.60 mmol, 735.3 mg), FAI (1.31 mmol, 224.4 mg), MABr (0.15 mmol, 16.2 mg), and CsI (0.08 mmol, 19.8 mg) – Cs<sub>0.05</sub>FA<sub>0.85</sub>MA<sub>0.10</sub>Pb(I<sub>0.97</sub>Br<sub>0.03</sub>)<sub>3</sub> – with 5% excess of PbI<sub>2</sub> in 1 mL of mixed solution of DMF and DMSO [DMF (v):DMSO (v) = 4:1] under mild heating conditions at

~70 °C to assist in dissolving. The perovskite precursor solution was deposited on the freshly prepared FTO/c-TiO<sub>2</sub>/m-TiO<sub>2</sub> substrate with a two-step spin-coating method. The first step was carried out at 2000 rpm with an acceleration rate of 200 rpm/s for 10 s. The second step followed at 6000 rpm with an acceleration rate of 2000 rpm/s for 30 s. CB (100 µL) was slowly dripped at the 15 s before the end of the second step. After this, the substrate was annealed at 120 °C for 20 min.

**Interface passivation Interface:** Following the annealing of the perovskite layer, the substrates were cooled down to room temperature. A 100 µL of OAI at 3 mg/mL (IPA) were deposited in the substrates while they were spin-coated at 5000 rpm for 30 s and heated at 100 °C for 5 min.

**Hole-transporting layer:** Spiro-OMeTAD, **4**, **7**, and **10** were dissolved in CB with a concentration of 75 mM. To add dopants, 1 mL of each HTM was doped by 20.6 µL Li-TFSI (520 mg/mL in acetonitrile) and 35.5 µL 4-*t*BP. The doped and undoped HTM solutions were spin-coated on the surface of the perovskite at 4000 rpm for 20 s with an acceleration rate of 2000 rpm/s.

**Gold electrode:** We finally evaporated a gold electrode under vacuum to form an 80 nm layer.

**Bilayer film preparation:** A perovskite layer, with the same composition as described above, was deposited on top of glass following the same spin-coating and annealing program as mentioned in the substrate preparation. Spiro-OMeTAD and HTMs **4**, **7**, and **10** were dissolved in CB with a concentration of 75 mM. To add dopants, 1 mL of each HTM was doped by 20.6 µL Li-TFSI (520 mg/mL in acetonitrile) and 35.5 µL 4-*t*BP. The doped and undoped HTM solutions were spin-coated on the surface of the perovskite at 700 rpm for 30 s with an acceleration rate of 100 rpm/s to yield a higher thickness for each HTM layer. Finally, an 80 nm layer of gold was thermally evaporated on top of the HTM layer.



## Synthetic procedures

### 2,6-Dibromo-4-(2'-bromothien-3'-yl)-4H-dithieno[3,2-b:2',3'-d]pyrrole (2)

4-(Thien-3'-yl)-DTP **1** (300 mg, 1.14 mmol) was dissolved in dry THF (12 mL) in a 50 mL 2-necked flask and cooled to  $-15^{\circ}\text{C}$ . NBS (625 mg, 3.05 mmol) was added under exclusion of light and the reaction mixture stirred for 2 h. Subsequently, water (25 mL) was added and the mixture extracted three times with DCM (20 mL). The combined organic phases were washed twice with water (25 mL), dried over  $\text{MgSO}_4$ , filtered, and evaporated. The crude product was purified via column chromatography on silica gel with PE/DCM 9:1 to yield tribrominated DTP **2** (330 mg, 0.66 mmol, 58%) as a colourless solid. Mp  $161.8-164.1^{\circ}\text{C}$ ;  $^1\text{H}$  NMR ( $\text{CDCl}_3$ , 400 MHz):  $\delta = 7.44$  (d,  $J = 5.8$  Hz, 1 H,  $\text{H}_5'$ ),  $7.02$  (d,  $J = 5.8$  Hz, 1 H,  $\text{H}_4'$ ),  $6.98$  (s, 2 H,  $\text{H}_3$ ) ppm;  $^{13}\text{C}$  NMR ( $\text{CDCl}_3$ , 101 MHz):  $\delta = 142.3, 137.4, 128.5, 126.6, 117.8, 116.9, 111.5, 108.2$  ppm; HRMS (MALDI):  $m/z$   $[\text{M}]^+$ , calcd. for  $\text{C}_{12}\text{H}_4\text{Br}_3\text{NS}_3$ , 494.7056, found 494.7048,  $\delta m/m = 1.60$  ppm.

### 4,4',4''-[4-(Thien-3'-yl)-4H-dithieno[3,2-b:2',3'-d]pyrrole-2,6,2'-triyl]tris[*N,N*-bis(4-methoxyphenyl)aniline] (4)

Tribromide **2** (250 mg, 0.50 mmol) was dissolved in THF (5 mL) and deaerated with Argon. Then, 4-methoxy-*N*-(4-methoxyphenyl)-*N*-[4-(4,4,5,5-tetramethyl-1,3,2-dioxaborolan-2-yl)phenyl]aniline **3** (760 mg, 1.76 mmol), tetrakis(triphenylphosphine)palladium(0) (87 mg, 0.08 mmol, 15 mol-%), and a 2 M solution of tripotassium phosphate solution in water (3.75 mL) were added. Subsequently, the reaction mixture was heated at  $85^{\circ}\text{C}$  for 18 h in a closed vial. The reaction was stopped by adding water (50 mL) and DCM (75 mL). The phases were separated and the aqueous phase was extracted three times with DCM (30 mL each). The combined organic phases were dried over magnesium sulfate, filtered, and the solvent removed in vacuo. The raw product was redissolved in DCM and filtered over aluminum oxide (activity II) and purified with preparative HPLC (silica gel, nitrophenyl-modified, *n*-hexane/DCM 3:7). DTP **4** (234 mg, 0.20 mmol, 40%) was isolated as a yellow solid. Mp  $148^{\circ}\text{C}$  (decomposition);  $^1\text{H}$  NMR (400 MHz,  $\text{THF}-d_8$ ):  $\delta = 7.50$  (d,  $J = 5.4$  Hz, 1 H,  $\text{H}_2$ ),  $7.37$  (bs, 4H, Ar-H),  $7.34$  (d,  $J = 5.4$  Hz, 1 H,  $\text{H}_3$ ),  $7.05-6.99$  (m, 8H, Ar-H),  $6.99-6.95$  (m, 2 H, Ar-H),  $6.92$  (bs, 2 H, Ar-H),  $6.89-6.80$  (m, 16H, Ar-H),  $6.75-6.64$  (m, 6H, Ar-H),  $3.75$  (s, 12 H, O- $\text{CH}_3$ ),  $3.71$  (s, 6H, O- $\text{CH}_3'$ ) ppm;  $^{13}\text{C}$  NMR (400 MHz,  $\text{THF}-d_8$ ):  $\delta = 142.7, 141.6, 130.53, 122.6, 118.6, 116.5, 112.2, 109.3$  ppm; HRMS (MALDI):  $m/z$   $[\text{M}]^+$ , calcd. for  $\text{C}_{72}\text{H}_{58}\text{N}_4\text{O}_6\text{S}_3$ , 1170.3493, found 1170.3507,  $\delta m/m = 1.23$  ppm.

### 2,6-Dibromo-4-(5'-bromothien-2'-yl)-4H-dithieno[3,2-b:2',3'-d]pyrrole (6)

4-(Thien-2'-yl)-DTP **5** (350 mg, 1.34 mmol) was dissolved in dry THF (7.5 mL) in a 50 mL 2-necked flask and cooled to  $-15^{\circ}\text{C}$ . NBS (725 mg, 3.50 mmol) was added under exclusion of light and the reaction mixture stirred for 2 hrs. Subsequently, a water/methanol mixture (15 mL 2:1) was added and the formed precipitate was filtrated and washed three times with a water/methanol mixture (2 mL 2:1) and dried in vacuo. Tribrominated DTP **6** (605 mg, 1.19 mmol, 89%) was isolated as a colourless solid. Mp  $209.2-212.8^{\circ}\text{C}$ ;  $^1\text{H}$  NMR ( $\text{CDCl}_3$ , 400 MHz):  $\delta = 7.34$  (s, 2 H,  $\text{H}_3$ ),  $7.18$  (d,  $J = 4.0$  Hz, 1 H,  $\text{H}_4'$ ),  $7.08$  (d,  $J = 4.0$  Hz, 1 H,  $\text{H}_3'$ ) ppm;  $^{13}\text{C}$  NMR ( $\text{CDCl}_3$ , 101 MHz):  $\delta = 142.7, 141.6, 130.53, 122.6, 118.6, 116.5, 112.2, 109.3$  ppm; HRMS (MALDI):  $m/z$   $[\text{M}]^+$ , calcd. for  $\text{C}_{12}\text{H}_4\text{Br}_3\text{NS}_3$ , 494.7056, found 494.7049,  $\delta m/m = 1.48$  ppm.

### 4,4',4''-[4-(Thien-2'-yl)-4H-dithieno[3,2-b:2',3'-d]pyrrole-2,6,5'-triyl]-tris[*N,N*-bis(4-methoxyphenyl)aniline] (7)

In the same way as for DTP **4**, tribromide **6** (500 mg, 1.00 mmol) in THF (12.5 mL), 4-methoxy-*N*-(4-methoxyphenyl)-*N*-[4-(4,4,5,5-tetramethyl-1,3,2-dioxaborolan-2-yl)phenyl]aniline **3** (1.51 g, 3.51 mmol), tetrakis(triphenylphosphine)palladium(0) (174 mg, 0.15 mmol, 15 mol%), and tripotassium phosphate (7.5 mL) were reacted at  $85^{\circ}\text{C}$  for 18 h in a closed vial. The reaction was stopped by adding water (50 mL) and DCM (75 mL). The phases were separated and the aqueous phase was extracted three times with DCM (30 mL each). The combined organic phases were dried over magnesium sulfate, filtered, and the solvent removed in vacuo. The crude product was purified via column chromatography on silica gel with PE/DCM 1:1 and size exclusion chromatography in THF. DTP **7** (220 mg, 0.19 mmol, 19%) was isolated as a yellow solid. Mp  $137^{\circ}\text{C}$  (decomposition);  $^1\text{H}$  NMR (400 MHz,  $\text{THF}-d_8$ ):  $\delta = 7.51-7.42$  (m, 10H, Ar-H),  $7.22$  (d,  $J = 3.9$  Hz, 1 H,  $\text{H}_4$ ),  $7.20$  (d,  $J = 3.9$  Hz, 1 H,  $\text{H}_3$ ),  $7.08-7.01$  (m, 16 H, Ar-H),  $6.93-6.81$  (m, 25 H, Ar-H),  $3.76$  (s, 6 H, O- $\text{CH}_3'$ ),  $3.75$  (s, 12 H, O- $\text{CH}_3$ ) ppm;  $^{13}\text{C}$  NMR (101 MHz,  $\text{THF}-d_8$ ):  $\delta = 157.5, 157.4, 149.7, 149.3, 145.7, 143.8, 141.6, 141.5, 140.0, 128.5, 127.6, 127.4, 126.8, 126.7, 125.9, 121.4, 121.2, 121.2, 116.4, 115.6, 115.5, 107.8, 55.6$  ppm; HRMS (MALDI):  $m/z$   $[\text{M}]^+$ , calcd. for  $\text{C}_{72}\text{H}_{58}\text{N}_4\text{O}_6\text{S}_3$ , 1170.3493, found 1170.3503,  $\delta m/m = 0.91$  ppm.

### 4,4',4'',4'''-[4-hexyl)-4H-dithieno[3,2-b:2',3'-d]pyrrole-2,3,5,6-tetrayl]-tetra[*N,N*-bis(4-methoxyphenyl)aniline] (10)

Tetrabrominated DTP **9** (200 mg, 0.35 mmol) was dissolved in THF (5 mL) and deaerated with argon. Then, 4-methoxy-*N*-(4-methoxyphenyl)-*N*-[4-(4,4,5,5-tetramethyl-1,3,2-dioxaborolan-2-yl)phenyl]aniline **3** (655 mg, 1.52 mmol), tet-

rakis(triphenylphosphine)palladium(0) (60 mg, 0.05 mmol, 15 mol%), and a 2 M solution of tripotassium phosphate solution in water (2.6 mL) were added. Subsequently, the reaction mixture was heated at 85 °C for 18 h in a closed vial. The reaction was stopped by adding water (50 mL) and DCM (75 mL). The phases were separated and the aqueous phase was extracted three times with DCM (30 mL each). The combined organic phases were dried over magnesium sulfate, filtered, and the solvent removed in vacuo. The raw product was redissolved in DCM and filtered over aluminum oxide (activity II) and purified with preparative HPLC (silica gel, nitrophenyl-modified, *n*-hexane/DCM 3:7). DTP **10** (260 mg, 0.18 mmol, 51 %) was isolated as a yellow solid. Mp 251.9–253.2 °C; <sup>1</sup>H NMR (400 MHz, THF-*d*<sub>8</sub>): δ = 7.08–7.01 (m, 4 H, Ar-H), 7.01–6.94 (m, 4 H, Ar-H), 6.91 (m, 16 H, Ar-H), 6.79 (m, 4 H, Ar-H), 6.76–6.68 (m, 16 H, Ar-H), 6.63–6.55 (m, 4 H, Ar-H), 3.64 (s, 12 H, O-CH<sub>3</sub>), 3.64 (s, 12 H, O-CH<sub>3</sub>'), 3.39 (t, *J* = 8.4 Hz, 2 H, CH<sub>2</sub>-α), 1.14–1.04 (m, 4 H, CH<sub>2</sub>-β,δ), 0.87 (p, *J* = 7.6 Hz, 2 H, CH<sub>2</sub>-ε), 0.74 (t, *J* = 7.3 Hz, 3 H, CH<sub>2</sub>-ζ), 0.57 (p, *J* = 7.4 Hz, 2 H, CH<sub>2</sub>-γ) ppm; <sup>13</sup>C NMR (101 MHz, THF-*d*<sub>8</sub>): δ = 156.4, 148.4, 147.5, 143.6, 140.6, 140.5, 131.1, 128.6, 127.6, 127.0, 126.7, 126.6, 123.6, 119.6, 119.2, 114.5, 114.5, 112.7, 54.6, 44.7, 31.3, 31.1, 26.3, 22.6, 13.6 ppm; HRMS (MALDI): *m/z* [M]<sup>+</sup>, calcd. for C<sub>94</sub>H<sub>85</sub>N<sub>5</sub>O<sub>8</sub>S<sub>2</sub>, 1475.5840, found 1475.5824, δ*m/m* = 1.08 ppm.

## Acknowledgment

M.A. and A.A. gratefully acknowledge King Abdulaziz City for Science and Technology (KACST) for their fellowship.

## Supporting Information

Materials and characterization details, synthetic procedures, NMR spectra, MS spectra, cyclic voltammograms, scanning electron microscopy (SEM) images, calculation of the quasi-Fermi level splitting, conductivity, and mobility measurements are given in the Supporting Information. Supporting Information for this article is available online at <https://doi.org/10.1055/a-1972-5978>.

## Conflict of Interest

The authors declare no conflict of interest.

## References

- (1) Lorenz, C.; Vogt, A.; Millan, J.; Mena-Osteritz, E.; Bäuerle P. *Org. Mater.* **2023**, *5*, 35.
- (2) Kojima, A.; Teshima, K.; Shirai, Y.; Miyasaka, T. *J. Am. Chem. Soc.* **2009**, *131*, 6050.
- (3) Best Research-Cell Efficiencies, <https://www.nrel.gov/pv/assets/pdfs/best-research-cell-efficiencies-rev220126b.pdf> (accessed November 11, 2022).
- (4) Leguy, A. M. A.; Frost, J. M.; McMahon, A. P.; Sakai, V. G.; Kochelmann, W.; Law, C.; Li, X.; Foglia, F.; Walsh, A.; O'Regan, B. C.; Nelson, J.; Cabral, J. T.; Barnes, P. R. F. *Nat. Commun.* **2015**, *6*, 1.
- (5) Li, W.; Wang, Z.; Deschler, F.; Gao, S.; Friend, R. H.; Cheetham, A. K. *Nat. Rev. Mater.* **2017**, *2*, 1.
- (6) Li, Y.; Zhou Liu, F.; Waqas, M.; Lun Leung, T.; Won Tam, H.; Qi Lan, X.; Tu, B.; Chen, W.; Djurišić, A. B.; Bing He, Z. *Small Methods* **2018**, *2*, 1700387.
- (7) Ji, L. J.; Sun, S. J.; Qin, Y.; Li, K.; Li, W. *Coord. Chem. Rev.* **2019**, *391*, 15.
- (8) Juarez-Perez, E. J.; Wußler, M.; Fabregat-Santiago, F.; Lakus-Wollny, K.; Mankel, E.; Mayer, T.; Jaegermann, W.; Mora-Sero, I. *J. Phys. Chem. Lett.* **2014**, *5*, 680.
- (9) Park, N.-G. *Mater. Today* **2015**, *18*, 65.
- (10) Zhang, W. E. I.; Saliba, M.; Stranks, S. D.; Sun, Y.; Shi, X.; Wiesner, U.; Snaith, H. J. *Nano Lett.* **2013**, *13*, 4505.
- (11) Ponseca Jr, C. S.; Savenije, T. J.; Abdellah, M.; Zheng, K.; Yartsev, A.; Pascher, T.; Harlang, T.; Chabera, P.; Pullerits, T.; Stepanov, A. *J. Am. Chem. Soc.* **2014**, *136*, 5189.
- (12) Xing, G.; Mathews, N.; Sun, S.; Lim, S. S.; Lam, Y. M.; Grätzel, M.; Mhaisalkar, S.; Sum, T. C. *Science* **2013**, *342*, 344.
- (13) Stranks, S. D.; Eperon, G. E.; Grancini, G.; Menelaou, C.; Alcocer, M. J. P.; Leijtens, T.; Herz, L. M.; Petrozza, A.; Snaith, H. J. *Science* **2013**, *342*, 341.
- (14) Constantinos, S.; Christos, M.; Mercouri, K. *Inorg. Chem.* **2013**, *52*, 9019.
- (15) Yoo, J. J.; Seo, G.; Chua, M. R.; Park, T. G.; Lu, Y.; Rotermund, F.; Kim, Y.-K.; Moon, C. S.; Jeon, N. J.; Correa-Baena, J.-P.; Bulović, V.; Shin, S. S.; Bawendi, M. G.; Seo, J. *Nature* **2021**, *590*, 587.
- (16) Kim, M.; Jeong, J.; Lu, H.; Lee, T. K.; Eickemeyer, F. T.; Liu, Y.; Choi, I. W.; Choi, S. J.; Jo, Y.; Kim, H. B.; Mo, S. I.; Kim, Y. K.; Lee, H.; An, N. G.; Cho, S.; Tress, W. R.; Zakeeruddin, S. M.; Hagfeldt, A.; Kim, J. Y.; Grätzel, M.; Kim, D. S. *Science* **2022**, *375*, 302.
- (17) Bauer, M.; Zhu, H.; Baumeler, T.; Liu, Y.; Eickemeyer, F. T.; Lorenz, C.; Mena-Osteritz, E.; Hertel, D.; Olthof, S.; Zakeeruddin, S. M.; Meerholz, K.; Grätzel, M.; Bäuerle, P. *Adv. Energy Mater.* **2021**, *11*, 2003953.
- (18) Murugan, P.; Hu, T.; Hu, X.; Chen, Y. J. *Mater. Chem. A* **2022**, *10*, 5044.
- (19) Nakka, L.; Cheng, Y.; Aberle, A. G.; Lin, F. *Adv. Energy Sustainability Res.* **2022**, *3*, 2200045.
- (20) Cheng, F.; Cao, F.; Fan, F. R.; Wu, B. *ChemSusChem* **2022**, *2022*, e202200340.
- (21) Mahajan, P.; Padha, B.; Verma, S.; Gupta, V.; Datt, R.; Tsoi, W. C.; Satapathi, S.; Arya, S. J. *Energy Chem.* **2022**, *68*, 330.
- (22) Zhang, X.; Steckler, T. T.; Dasari, R. R.; Ohira, S.; Potscavage, W. J.; Tiwari, S. P.; Coppée, S.; Ellinger, S.; Barlow, S.; Brédas, J.-L.; Kippelen, B.; Reynolds, J. R.; Marder, S. R. *J. Mater. Chem.* **2010**, *20*, 123.
- (23) Lu, H.-I.; Lu, C.-W.; Lee, Y.-C.; Lin, H.-W.; Lin, L.-Y.; Lin, F.; Chang, J.-H.; Wu, C.-I.; Wong, K.-T. *Chem. Mater.* **2014**, *26*, 4361.
- (24) (a) Rasmussen, S. C.; Evenson, S. J. *Prog. Polym. Sci.* **2013**, *38*, 1773. (b) Ogawa, K. Dissertation; North Dakota State University, **2005**.
- (25) Yin, X.; Zhou, J.; Song, Z.; Dong, Z.; Bao, Q.; Shrestha, N.; Bista, S. S.; Ellingson, R. J.; Yan, Y.; Tang, W. *Adv. Funct. Mater.* **2019**, *29*, 1904300.

- (26) Cao, J.; Du, F.; Yang, L.; Tang, W. *J. Mater. Chem. A* **2020**, *8*, 22572.
- (27) Sandoval-Torrientes, R.; Zimmermann, I.; Calbo, J.; Aragón, J.; Santos, J.; Ortí, E.; Martín, N.; Nazeeruddin, M. K. *J. Mater. Chem. A* **2018**, *6*, 5944.
- (28) Wu, B.; Fu, Q.; Sun, L.; Liu, Y.; Sun, Z.; Xue, S.; Liu, Y.; Liang, M. *ACS Energy Lett.* **2022**, *7*, 2667.
- (29) Vogt, A.; Schwer, F.; Förtsch, S.; Lorenz, C.; Mena-Osteritz, E.; Aubele, A.; Kraus, T.; Bäuerle, P. *Chem. Eur. J.* **2021**, *27*, 12362.
- (30) Leijtens, T.; Ding, I. K.; Giovenzana, T.; Bloking, J. T.; McGehee, M. D.; Sellinger, A. *ACS Nano* **2012**, *6*, 1455.
- (31) Li, H.; Lambert, C. *Chem. Eur. J.* **2006**, *12*, 1144.
- (32) Saliba, M.; Matsui, T.; Seo, J.-Y.; Domanski, K.; Correa-Baena, J.-P.; Nazeeruddin, M. K.; Zakeeruddin, S. M.; Tress, W.; Abate, A.; Hagfeldt, A.; Grätzel, M. *Energy Environ. Sci.* **2016**, *9*, 1989.
- (33) Bai, S.; Da, P.; Li, C.; Wang, Z.; Yuan, Z.; Fu, F.; Kaweck, M.; Liu, X.; Sakai, N.; Wang, J. T.-W.; Huettner, S.; Buecheler, S.; Fahlman, M.; Gao, F.; Snaith, H. J. *Nature* **2019**, *571*, 245.
- (34) Zhu, H.; Liu, Y.; Eickemeyer, F. T.; Pan, L.; Ren, D.; Ruiz-Preciado, M. A.; Carlsen, B.; Yang, B.; Dong, X.; Wang, Z.; Liu, H.; Wang, S.; Zakeeruddin, S. M.; Hagfeldt, A.; Dar, M. I.; Li, X.; Grätzel, M. *Adv. Mater.* **2020**, *32*, 1907757.
- (35) Tang, S.; Huang, S.; Wilson, G. J.; Ho-Baillie, A. *Trends Chem.* **2020**, *2*, 638.
- (36) Kim, M.; Kim, G. H.; Lee, T. K.; Choi, I. W.; Choi, H. W.; Jo, Y.; Yoon, Y. J.; Kim, J. W.; Lee, Y.; Huh, D.; Lee, H.; Kwak, S. K.; Kim, J. Y.; Kim, D. S. *Joule* **2019**, *3*, 2179.
- (37) Lu, H.; Liu, Y.; Ahlawat, P.; Mishra, A.; Tress, W. R.; Eickemeyer, F. T.; Yang, Y.; Fu, F.; Wang, Z.; Avalos, C. E.; Carlsen, B. I.; Agarwalla, A.; Zhang, X.; Zhan, Y.; Zakeeruddin, S. M.; Emsley, L.; Rothlisberger, U.; Zheng, L.; Hagfeldt, A.; Grätzel, M. *Science* **2020**, *370*, eabb8985.
- (38) Yuan, R.; Cai, B.; Li, Y.; Gao, X.; Gu, Y.; Fan, Z.; Liu, X.; Yang, C.; Liu, M.; Zhang, W.-H. *Energy Environ. Sci.* **2021**, *14*, 5074.
- (39) Guo, P.; Zhu, H.; Zhao, W.; Liu, C.; Zhu, L.; Ye, Q.; Jia, N.; Wang, H.; Zhang, X.; Huang, W.; Vinokurov, V. A.; Ivanov, E.; Shchukin, D.; Harvey, D.; Ulloa, J. M.; Hierro, A.; Wang, H. *Adv. Mater.* **2021**, *33*, 2101590.
- (40) Jeong, J.; Kim, M.; Seo, J.; Lu, H.; Ahlawat, P.; Mishra, A.; Yang, Y.; Hope, M. A.; Eickemeyer, F. T.; Kim, M.; Yoon, Y. J.; Choi, I. W.; Darwich, B. P.; Choi, S. J.; Jo, Y.; Lee, J. H.; Walker, B.; Zakeeruddin, S. M.; Emsley, L.; Rothlisberger, U.; Hagfeldt, A.; Kim, D. S.; Grätzel, M.; Kim, J. Y. *Nature* **2021**, *592*, 381.
- (41) Kirchartz, T.; Márquez, J. A.; Stolterfoht, M.; Unold, T. *Adv. Energy Mater.* **2020**, *10*, 1904134.
- (42) Ross, R. T. *J. Chem. Phys.* **1967**, *46*, 4590.
- (43) Caprioglio, P.; Stolterfoht, M.; Wolff, C. M.; Unold, T.; Rech, B.; Albrecht, S.; Neher, D. *Adv. Energy Mater.* **2019**, *9*, 1901631.
- (44) Tress, W. Maximum Efficiency and Open-Circuit Voltage of Perovskite Solar Cells, In Organic-Inorganic Halide Perovskite Photovoltaics, Park, N.-G.; Grätzel, M.; Miyasaka, T.; Springer: Berlin, **2016**; 53.
- (45) Marinova, N.; Tress, W.; Humphry-Baker, R.; Dar, M. I.; Bojinov, V.; Zakeeruddin, S. M.; Nazeeruddin, M. K.; Grätzel, M. *ACS Nano* **2015**, *9*, 4200.
- (46) Correa-Baena, J.-P.; Tress, W.; Domanski, K.; Anaraki, E. H.; Turren-Cruz, S.-H.; Roose, B.; Boix, P. P.; Grätzel, M.; Saliba, M.; Abate, A. *Energy Environ. Sci.* **2017**, *10*, 1207.
- (47) Do Kim, H.; Ohkita, H. *Sol. RRL* **2017**, *1*, 1700027.
- (48) Wu, N.; Wu, Y.; Walter, D.; Shen, H.; Duong, T.; Grant, D.; Barugkin, C.; Fu, X.; Peng, J.; White, T.; Catchpole, K.; Weber, K. *Energy Technol.* **2017**, *5*, 1827.
- (49) Ma, C.; Park, N.-G. *Chem* **2020**, *6*, 1254.
- (50) Abate, A.; Leijtens, T.; Pathak, S.; Teuscher, J.; Avolio, R.; Errico, M. E.; Kirkpatrick, J.; Ball, J. M.; Docampo, P.; McPherson, I.; Snaith, H. J. *Phys. Chem. Chem. Phys.* **2013**, *15*, 2572.
- (51) Liu, Q.; Fan, L.; Zhang, Q.; Zhou, A.; Wang, B.; Bai, H.; Tian, Q.; Fan, B.; Zhang, T. *ChemSusChem* **2017**, *10*, 3098.
- (52) Wang, D.; Chen, S.-C.; Zheng, Q. *J. Mater. Chem. A* **2021**, *9*, 11778.
- (53) Burschka, J.; Dualah, A.; Kessler, F.; Baranoff, E.; Cevey-Ha, N.-L.; Yi, C.; Nazeeruddin, M. K.; Grätzel, M. *J. Am. Chem. Soc.* **2011**, *133*, 18042.
- (54) Snaith, H. J.; Grätzel, M. *Appl. Phys. Lett.* **2006**, *89*, 262114.
- (55) Li, Z.; Tinkham, J.; Schulz, P.; Yang, M.; Kim, D. H.; Berry, J.; Sellinger, A.; Zhu, K. *Adv. Energy Mater.* **2017**, *7*, 1601451.
- (56) Wang, S.; Yuan, W.; Meng, Y. S. *ACS Appl. Mater. Interfaces* **2015**, *7*, 24791.
- (57) Fabregat-Santiago, F.; Bisquert, J.; Cevey, L.; Chen, P.; Wang, M.; Zakeeruddin, S. M.; Grätzel, M. *J. Am. Chem. Soc.* **2009**, *131*, 558.
- (58) Ulfa, M.; Pauporté, T.; Bui, T.-T.; Goubard, F. *J. Phys. Chem. C* **2018**, *122*, 11651.
- (59) Tan, B.; Raga, S. R.; Chesman, A. S. R.; Furer, S. O.; Zheng, F.; McMeekin, D. P.; Jiang, L.; Mao, M.; Lin, X.; Wen, X.; Lu, J.; Cheng, Y.-B.; Bach, U. *Adv. Energy Mater.* **2019**, *9*, 1901519.
- (60) Forward, R. L.; Chen, K. Y.; Weekes, D. M.; Dvorak, D. J.; Cao, Y.; Berlinguette, C. P. *ACS Energy Lett.* **2019**, *4*, 2547.
- (61) Tan, B.; Raga, S. R.; Rietwyk, K. J.; Lu, J.; Furer, S. O.; Griffith, J. C.; Cheng, Y.-B.; Bach, U. *Nano Energy* **2021**, *82*, 105658.
- (62) Yang, S.; Chen, S.; Mosconi, E.; Fang, Y.; Xiao, X.; Wang, C.; Zhou, Y.; Yu, Z.; Zhao, J.; Gao, Y.; De Angelis, F.; Huang, J. *Science* **2019**, *365*, 473.
- (63) Kim, H.; Lee, S.-U.; Lee, D. Y.; Paik, M. J.; Na, H.; Lee, J.; Il Seok, S. *Adv. Energy Mater.* **2019**, *9*, 1902740.
- (64) Krishna, A.; Zhang, H.; Zhou, Z.; Gallet, T.; Dankl, M.; Ouellette, O.; Eickemeyer, F. T.; Fu, F.; Sanchez, S.; Mensi, M.; Zakeeruddin, S. M.; Rothlisberger, U.; Reddy, G. N. M.; Redinger, A.; Grätzel, M.; Hagfeldt, A. *Energy Environ. Sci.* **2021**, *14*, 5552.
- (65) Kim, H.-S.; Lee, C.-R.; Im, J.-H.; Lee, K.-B.; Moehl, T.; Marchioro, A.; Moon, S.-J.; Humphry-Baker, R.; Yum, J.-H.; Moser, J. E.; Grätzel, M.; Park, N.-G. *Sci. Rep.* **2012**, *2*, 1.
- (66) Urieta-Mora, J.; García-Benito, I.; Molina-Ontoria, A.; Martín N. *Chem. Soc. Rev.* **2018**, *47*, 8541.
- (67) Gao, P.; Cho, D.; Yang, X.; Enkelmann, V.; Baumgarten, M.; Müllen K. *Chem. Eur. J.* **2010**, *16*, 5119.